Longitudinal magnetoconductance and the planar Hall conductance in inhomogeneous Weyl semimetals

Azaz Ahmad [1], Karthik V. Raman,[2] Sumanta Tewari [3], and Gargee Sharma [1]
[1]*School of Physical Sciences, Indian Institute of Technology Mandi, Mandi 175005, India*
[2]*Tata Institute of Fundamental Research, Hyderabad, Telangana 500046, India*
[3]*Department of Physics and Astronomy, Clemson University, Clemson, South Carolina 29634, USA*

(Received 17 October 2022; revised 9 April 2023; accepted 12 April 2023; published 27 April 2023)

Elastic deformations (strain) couple to the electronic degrees of freedom in Weyl semimetals as an axial magnetic field (chiral gauge field), which in turn affects their impurity-dominated diffusive transport. Here we study the longitudinal magnetoconductance (LMC) in the presence of strain, Weyl cone tilt, and finite intervalley scattering, taking into account the momentum dependence of the scattering processes (both internode and intranode), as well as charge conservation. We show that strain-induced chiral gauge field results in "strong sign reversal" of the LMC, which is characterized by the reversal of orientation of the magnetoconductance parabola with respect to the magnetic field. On the other hand, external magnetic field results in "strong sign reversal," only for sufficiently strong intervalley scattering. When both external and chiral gauge fields are present, we observe both strong and weak sign reversal, where in the case of weak sign reversal, the rise and fall of magnetoconductivity depends on the direction of the magnetic field and/or the chiral gauge field, and is not correlated with the orientation of the LMC parabola. The combination of the two fields is shown to generate striking features in the LMC phase diagram as a function of various parameters such as tilt, strain, and intervalley scattering. We also study the effect of strain-induced chiral gauge field on the planar Hall conductance and highlight its distinct features that can be probed experimentally.

DOI: 10.1103/PhysRevB.107.144206

I. INTRODUCTION

Fermions and the atomic lattice form the building blocks of condensed matter. While each of them is fundamentally different from the other, the interplay between the two leads to remarkable effects. In recent works, massless Dirac fermions, which have resurged in condensed matter, have been shown to couple to the elastic deformations of the lattice (strain) as an axial magnetic field (also known as chiral gauge field). Prominent examples where such fields can be realized include graphene [1–3] and three-dimensional Weyl semimetals [4–6]. For instance, in graphene, the generated field can be even as large as 300 T, as observed via spectroscopic measurement of the Landau levels [7]. Measurement of strain-induced chiral magnetic field as well as its implications on electron transport in three-dimensional Weyl and Dirac semimetals materials is of high interest to the condensed matter community.

The reason why Weyl and Dirac semimetals also have been fascinating is due to some intriguing properties that are absent in conventional metals. Some examples include the anomalous Hall [8,9] and Nernst [10–12] effects, open Fermi arcs [13], planar Hall and Nernst effects [14,15], and the manifestation of chiral or Adler-Bell-Jackiw anomaly [16–25]. The origin of each of these effects can be traced down to the nontrivial topology of the Bloch bands. Specifically, the low-energy band structure of Weyl nodes comprises of pairs of nondegenerate massless Dirac cones that are topologically protected by the chirality quantum number (also known as the Chern number). Without any coupling to an external gauge field, the charge of a given chirality remains conserved. The conservation law is, however, broken when Weyl fermions are coupled to background gauge fields such as electric or magnetic fields [16–18]. This breakdown of conservation laws is known as "chiral anomaly," rooting its name from the particle physics literature. The verification of chiral anomaly in Weyl semimetals is a very active area of investigation in condensed matter physics.

In a minimal model of Weyl semimetal, Weyl nodes must be separated in momentum space by a vector $\mathbf{b}$ to ensure topological protection. Alternatively, the vector $\mathbf{b}$ can also be interpreted as an axial gauge field since it couples with an opposite sign to Weyl nodes of opposite chirality [25–29]. Thus, the spatial variation of $\mathbf{b}$ generates an axial magnetic field $\mathbf{B}_5 = \nabla \times \mathbf{b}$, which also couples oppositely to Weyl nodes of opposite chirality. An effective $\mathbf{B}_5$ field can emerge from an inhomogeneous strain profile in Weyl semimetals. In the presence of an effective chiral gauge field $\mathbf{B}_5$, the effective magnetic field experienced by Weyl fermions at a given node of chirality χ is $\mathbf{B} \longrightarrow \mathbf{B} + \chi \mathbf{B}_5$, where $\mathbf{B}$ is the external magnetic field. Therefore, the conservation laws are also modified accordingly in the presence of the $\mathbf{B}_5$ field. Recent works have pointed out that even in the absence of an external magnetic field, the chiral gauge field influences the diffusive electron transport in Weyl semimetals by modifying its longitudinal magnetoconductance (LMC) [6] as well as the planar Hall conductance (PHC) [30]. Although true in spirit, the drawback of these works is that they ignore the momentum

dependence of scattering when the Weyl fermions scatter within a node (known as intranode scattering or intravalley scattering) conserving both the total charge and chiral charge and also when they scatter to the other node (internode and intervalley scattering), in which case they conserve only the total charge. Moreover, intervalley scattering, which is the essence of "true chiral anomaly," has been neglected in Ref. [30]. In a recent work [31], some of the co-authors of this work have pointed out that momentum dependence of scattering, as well as charge conservation constraint, can lead to drastic differences in the qualitative conclusions. It is therefore of immense importance to correctly treat the effect of strain-induced gauge field on electron transport in Weyl semimetals, which is the focus of this work.

In this work, we critically examine the effect of strain-induced chiral gauge field via the Boltzmann formalism (thus limiting ourselves to only weak perturbative fields) on two linear response quantities: the longitudinal magnetoconductance and the planar Hall conductance. We study these effects in both time-reversal breaking Weyl semimetals (WSM) (with and without tilt) as well as inversion asymmetric Weyl semimetals. Earlier it was believed that positive longitudinal magnetoconductivity must manifest from chiral anomaly at least in the limit of weak external magnetic field, but this claim was corrected later on when sufficiently strong intervalley scattering was shown to switch the sign of longitudinal magnetoconductivity even in the weak-$\mathbf{B}$ limit [32]. Typically, by positive (negative) longitudinal magnetoconductance we mean that $[\sigma(|\mathbf{B}|) - \sigma(\mathbf{B}=0)] > (<)\ 0$, i.e., the field-dependent conductivity is greater (smaller) than the zero-field conductivity. Here we show that the presence of $\mathbf{B}_5$ field can also reverse the sign of LMC, but *only* along a particular direction of the magnetic field (see Fig. 2). This leads to an interesting scenario of the LMC being positive along one direction of the magnetic field and negative when the direction of the magnetic field is reversed. To counter this ambiguity in the sign of LMC, we introduce the idea of weak sign reversal and strong sign reversal, which depends on the orientation and the vertex of the parabola of magnetoconductivity with respect to the magnetic field [Eq. (3)]. We show that in the presence of only strain-induced chiral gauge field (and absence of external magnetic field), the system shows signatures of strong sign reversal for all values of intervalley scattering. In the presence of only the external magnetic field (and the absence of a chiral gauge field), the system shows strong sign reversal only at sufficiently large values of scattering. In the presence of both chiral gauge and externally applied magnetic field, signatures of both weak and strong sign reversal are observed and, furthermore, very interesting features emerge in the phase diagram of LMC as a function of various system parameters such as the intervalley scattering, tilt, and strain. We point out that throughout this paper, whenever the external magnetic field is absent, we discuss weak and strong sign reversal in the context of the LMC parabola with respect to the chiral gauge field $\mathbf{B}_5$. When the external magnetic field is present (in either presence or absence of the chiral gauge field), weak and strong sign reversal is discussed in the context of the LMC parabola with respect to the external magnetic field $\mathbf{B}$. Tables I and II provide a succinct summary of the main results for a TR broken Weyl semimetal. We also extend the idea of weak and strong sign reversal to the planar Hall conductance as well, and study the effect of strain-induced gauge field on the same. Along with other features, we also unravel a very interesting behavior in the planar Hall conductance due to an interplay between the chiral gauge field and the external magnetic field. Specifically, we observe a region in the parameter space where the planar Hall conductivity increases in magnitude upon increasing the scattering strength, which is counterintuitive.

TABLE I. Summary for the type of the change: weak (W), strong (S), and weak and strong (WS) in the sign for the LMC under different cases for a TR broken WSM. For B and B_5, 0 and 1 indicate the absence and presence of the fields, respectively. For tilt, -1 indicates the tilt of the Weyl cones are oppositely oriented, $+1$ indicates orientation in the same direction, and 0 indicates no tilting. When $B = 0$, sign change of LMC is with respect to the B_5 field, and whenever $B = 1$, the sign change is with respect to the B field irrespective of B_5. This table corresponds to the case when $\alpha < \alpha_c$.

Tilt	B	B_5	Sign reversal
0	1	0	
0	0	1	S
0	1	1	W
1	1	0	
1	0	1	WS
1	1	1	W
-1	1	0	W
-1	0	1	WS
-1	1	1	W

This paper is organized as follows. In Sec. II, we introduce the concept of weak and strong sign reversal using a minimal model of a TR broken untilted WSM. We also study the interplay of strain, tilt, and intervalley scattering on LMC and PHC. In Sec. III we extend our results to a TR broken tilted Weyl semimetal. In Sec. IV, we present the results for inversion asymmetric Weyl semimetals. Section V is devoted to a brief discussion on the inclusion of inhomogeneities in strain-induced chiral gauge field. We conclude in Sec. VI. All the calculations are relegated to the Appendix.

TABLE II. Summary for the type of the change: weak (W), strong (S), and weak and strong (WS) in the sign for the LMC under different cases for a TR broken WSM. This table corresponds to the case when $\alpha > \alpha_c$. All abbreviations are same as in Table I.

Tilt	B	B_5	Sign reversal
0	1	0	S
0	0	1	S
0	1	1	WS
1	1	0	S
1	0	1	WS
1	1	1	WS
-1	1	0	WS
-1	0	1	WS
-1	1	1	WS

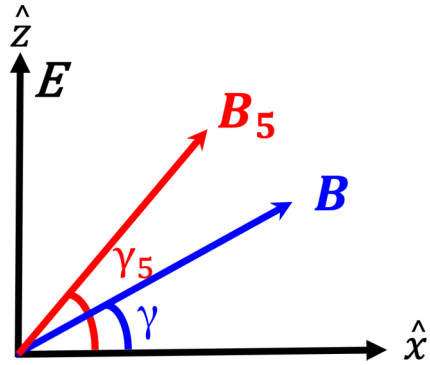

FIG. 1. Spatial orientation of electric and magnetic fields. Here **B** is the external magnetic field and $\mathbf{B_5}$ strain-induced chiral gauge field, γ and γ_5 are their angles measured from the increasing x direction, i.e., $\mathbf{B} = B(\cos\gamma, 0, \sin\gamma)$ and $\mathbf{B_5}^{\chi} = \chi B_5(\cos\gamma_5, 0, \sin\gamma_5)$. Therefore, **B** and $\mathbf{B_5}$ are constrained to be in the x-z plane. We have fixed the direction of electric field along increasing z direction.

II. TIME-REVERSAL BROKEN UNTILTED WEYL SEMIMETALS

We consider a minimal model of a time-reversal symmetry broken Weyl semimetal, i.e., two linearly dispersing nondegenerate Weyl cones separated in momentum space. We also assume that there is no tilting of the Weyl cones in any direction. The low-energy Hamiltonian is given by

$$H = \sum_{\chi} \sum_{\mathbf{k}} \chi \hbar v_F \mathbf{k} \cdot \boldsymbol{\sigma}. \tag{1}$$

Here $\chi = \pm 1$ is the chirality of the node, **k** is the momentum, v_F is the velocity parameter, and $\boldsymbol{\sigma}$ is the vector of Pauli spin matrices.

Using the quasiclassical Boltzmann theory, we study transport in Weyl semimetals in the limit of weak electric and magnetic fields. Since quasiclassical Boltzmann theory is valid away from the nodal point such that $\mu^2 \gg \hbar v_F^2 eB$, therefore, without any loss of generality we will assume that the chemical potential lies in the conduction band. Throughout this paper, we fix the direction of the applied external electric field to be along $+\hat{z}$, i.e., $\mathbf{E} = E\hat{z}$. Further, we rotate the magnetic field along the xz plane such that it makes an angle γ with respect to the $\hat{x}$ axis, i.e., $\mathbf{B} = B(\cos\gamma, 0, \sin\gamma)$. When $\gamma = \pi/2$, the electric and magnetic fields are parallel to each other. Similarly, the strain-induced chiral gauge field is rotated in the xz plane, i.e., $\mathbf{B_5}^{\chi} = \chi B_5(\cos\gamma_5, 0, \sin\gamma_5)$. The geometrical arrangement is presented in Fig. 1. The details of the Boltzmann calculations are relegated to the Appendix.

A. Longitudinal magnetoconductance in the absence of strain

First, we briefly discuss longitudinal magnetoconductance in the absence of strain-induced chiral gauge field B_5. Since this has been discussed in many earlier works, we will not elucidate in a detailed fashion. On application of a magnetic field parallel to the electric field, the longitudinal magnetoconductivity obtained in the semiclassical limit is expressed as

$$\sigma_{zz}(B) = \sigma_{zz}^{(2)} B^2 + \sigma_{zz}^{(0)}, \tag{2}$$

where $\sigma_{zz}^{(0)}$ is the conductivity in absence of any magnetic field, while $\sigma_{zz}^{(2)}$ is the quadratic coefficient of magnetic field dependence. In contrast to earlier anticipation that the quadratic coefficient $\sigma_{zz}^{(2)}$ is always positive, it was recently realized that the coefficient can become negative if the intervalley scattering is sufficiently strong [32]. In other words, large intervalley scattering results in negative longitudinal magnetoconductivity or reverses its sign. Specifically, this occurs above a critical intervalley scattering strength α_c, and the coefficient $\sigma_{zz}^{(2)}$ continuously goes from positive to negative around α_c. The sign of the parameter $\sigma_{zz}^{(2)}$ also correlates with increasing or decreasing longitudinal magnetoconductivity. We call this as the usual "*sign reversal*" of LMC, which refers to the fact that $\sigma_{zz}(|B|) - \sigma_{zz}(B = 0)$ continuously changes sign from positive to negative.

B. Longitudinal magnetoconductance in the presence of strain

Next, let us examine the behavior in the presence of an effective chiral gauge field (B_5) that may arise in inhomogeneous WSMs due to the presence of strain. The chiral gauge field couples oppositely in opposite valleys; thus, the net magnetic field becomes valley dependent, i.e., $B \to B + \chi B_5$. We first assume that B_5 is held parallel to the external magnetic field B, which in turn is parallel to the electric field. Figure 2 plots the behavior of $\delta\sigma_{zz}(B)$, which is the change in LMC due to the magnetic field, i.e., $\delta\sigma_{zz}(B) = \sigma_{zz}(B) - \sigma_{zz}(B = 0)$. We find that the increase or decrease of LMC depends on the direction of the magnetic field, especially close to $B = 0$. We find that LMC decreases for positive values of magnetic field and increases for negative values of magnetic field. Furthermore, when the magnitude of B is increased further away from zero, LMC increases (decreases) for both negative and positive values of B when $\alpha < \alpha_c$ ($\alpha > \alpha_c$). We contrast this to the behavior in the absence of strain, where the LMC either decreases (when $\alpha > \alpha_c$) or increases (when $\alpha < \alpha_c$) irrespective of the magnitude and the direction of the applied magnetic field. Hence, it turns out that stating whether the longitudinal magnetoconductance is only positive or negative for a given scenario, as often is the case in most of the experimental and theoretical literature, turns out to be rather ambiguous.

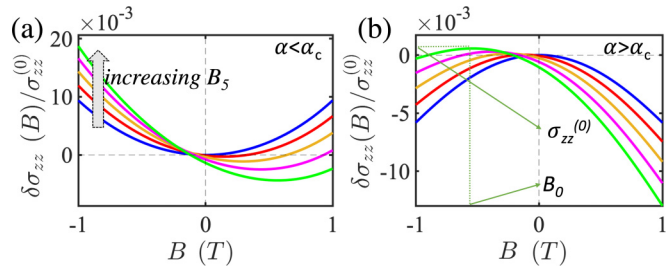

FIG. 2. Change in LMC $[\delta\sigma_{zz}(B)]$ with respect to the magnetic field for a minimal model of untilted TR broken WSM [Eq. (2)]. (a) Weak intervalley scattering ($\alpha < \alpha_c$), and (b) strong (and weak) intervalley scattering ($\alpha > \alpha_c$). As we move from blue to the green curve in both the plots (in the direction of the arrow), we increase B_5 from zero to 0.2 T. The B_5 field is held parallel to the external magnetic field. The vertex B_0 and the corresponding $\sigma_{zz}^{(0)}$ are marked for the green curve in plot (b).

1. Weak and strong sign reversal

To counter the above ambiguity, first, we generalize the expression of magnetoconductivity from Eq. (2) to the following:

$$\sigma_{zz}(B) = \sigma_{zz}^{(2)}(B - B_0)^2 + \sigma_{zz}^{(0)}. \tag{3}$$

The above definition allows us to shift the vertex of the parabola (B_0) away from the origin, which is essential to fit the results presented in Fig. 2. Now, in Fig. 2(a), when the strength of the intervalley scattering $\alpha < \alpha_c$, even though LMC is negative at low positive magnetic fields, it is in fact always positive when seen in reference to the vertex B_0, i.e., LMC is always positive when the change in the magnetic field and conductivity is seen with respect to the conductivity at B_0, and not with respect to the origin. We call this as *weak* sign reversal because the orientation of the parabola remains intact, only the vertex is shifted from the origin, and also $\sigma_{zz}^{(2)}$ remains positive. Thus, when intervalley scattering is weak, strain in inhomogeneous WSMs drives the system to the weak sign-reversed state along a particular direction of the magnetic field. In summary, the characteristics defining weak sign reversal are the following: (i) $B_0 \neq 0$, (ii) $\sigma_{zz}^{(0)} \neq \sigma_{zz}(B = 0)$, (iii) sign $\sigma_{zz}^{(2)} > 0$.

In Fig. 2(b), when the strength of the intervalley scattering is greater than the critical value (α_c), the orientation of the parabola is reversed, i.e., LMC decreases when seen with reference to B_0, and $\sigma_{zz}^{(2)}$ becomes negative. Due to this reason, we call this as *strong* sign reversal. Strong sign reversal is governed by the following condition: (i) sign $\sigma_{zz}^{(2)} < 0$, *without* any restriction to the values of B_0 and $\sigma_{zz}^{(0)}$. We then conclude that signatures of both strong and weak sign reversal would be (i) $B_0 \neq 0$, (ii) $\sigma_{zz}^{(0)} \neq \sigma_{zz}(B = 0)$, (iii) sign $\sigma_{zz}^{(2)} < 0$.

Since B_0 is shifted from the origin due to infinitesimal strain even when $\alpha > \alpha_c$, we conclude that sufficiently strong intervalley scattering along with strain in inhomogeneous WSMs drives the system to show signatures of both weak and strong sign reversal, as demonstrated in Fig. 2(b). In general, the chiral gauge may be oriented away from the z axis and rotated along the xz plane, and the variation of magnetoconductivity with respect to the angle γ_5 (the angle between x axis and the B_5 field) is straightforward to understand. As γ_5 increases from zero to $\pi/2$, the contribution due to to the chiral gauge field increases in a sinusoidal fashion. We do not explicitly plot this behavior.

We point out that strong sign reversal of LMC results from including energy shift due to the orbital magnetic moment (OMM) [31–35]. Importantly, the energy shift results in dissimilar Fermi surfaces due to the differing signs of the orbital magnetic moment at both valleys. In Weyl semimetals, chiral anomaly refers to the nonconservation of chiral charge in the presence of external gauge fields, i.e., a right-moving electron scatters to a left-moving state; the conductivity increases with an increasing magnetic field. The dissimilarity in the Fermi surfaces due to the OMM energy shift causes a right-moving state to scatter into a state that is no longer its left-mover partner state, as required by the chiral anomaly. Furthermore, increasing intervalley scattering strength results in a greater probability of mismatch of the Fermi surfaces, eventually reversing the LMC sign. Weak sign reversal, on the other hand, involves both intravalley and intervalley scattering. It is qualitatively different from strong sign reversal, and is not necessarily dependent on the orbital magnetic moment correction to the energy dispersion.

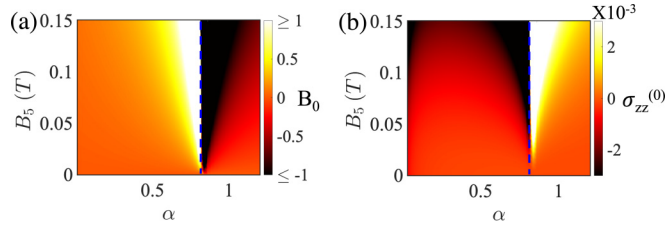

FIG. 3. (a) The vertex of the parabola B_0, and (b) conductivity at B_0 for a minimal model of untilted TR broken WSM [Eq. (2)]. Around the blue dashed contour ($\alpha = \alpha_c$) we see strong sign reversal. The parameters B_0 and $\sigma_{zz}^{(0)}$ show a striking change of sign as we move across the α_c contour.

2. Transition between weak and strong sign-reversed cases

In Fig. 3 we plot the parameters B_0 and $\sigma_{zz}^{(0)}$ as a function of the chiral gauge field and intervalley scattering strength. The transition from "weak" to "strong and weak" sign-reversed case is characterized by reversal in signs of the relative offset in conductivity $\sigma_{zz}^{(0)}$, as well as the vertex of the parabola B_0, i.e., $B_0 \leqslant 0$ when $\sigma_{zz}^{(0)} \geqslant 0$, and vice versa. In contrast, $\sigma_{zz}^{(2)}$ continuously interpolates across zero (not plotted). No discontinuity in B_0 or $\sigma^{(0)}$ is observed in the weak sign-reversed case, i.e., as the strain-induced field is increased from zero for a constant intervalley scattering, the parameters B_0 and $\sigma_{zz}^{(0)}$ vary continuously.

In Fig. 4 we plot the the longitudinal magnetoconductivity as a function of magnetic field for different values of intervalley scattering. An increase in intervalley scattering strength decreases the magnetoconductivity, i.e., $|\sigma_{zz}(B, \alpha)| > |\sigma_{zz}(B, \alpha + \epsilon)|$, where ϵ is the infinitesimal increase in the scattering strength, which is also expected on physical grounds. We find this feature remains intact even in the presence of strain-induced chiral gauge field, as shown in Fig. 4(b). We particularly highlight this point as this will be contrasted to the planar Hall conductivity that shows an anomalous increase in conductivity with increasing intervalley scattering strength. In Fig. 4(c) we plot the LMC in the presence of only chiral gauge magnetic field (i.e., $B = 0$). Since, in this case the external magnetic field is zero, positive (negative) LMC and weak (strong) sign reversal can only be defined with reference to the B_5 field. We find that the strain-induced chiral gauge field by itself only results in strong sign-reversed phase irrespective of the intervalley scattering strength. In Fig. 4(d) we plot LMC as a function of the chiral gauge field B_5, but in the presence of a fixed external magnetic field. The B_5 field results in strong sign-reversed phase and the additional external magnetic field results in weak sign-reversed phase as well.

3. Experimental implications

Experimentally, by tuning the applied strain on the material, one can realize the weak sign-reversed state; however, switching to the strong sign-reversed state requires tuning

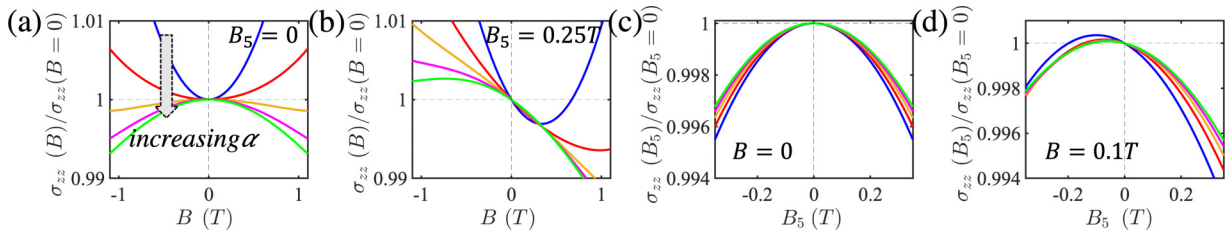

FIG. 4. Longitudinal magnetoconductivity for a minimal model of TR broken untilted Weyl semimetal. (a) Increasing intervalley scattering strength results in strong sign reversal. (b) In addition to this, infinitesimal strain now results in weak sign reversal as well. (c) When plotted as a function of the gauge field B_5, LMC is always strongly sign reversed. (d) In the presence of an external magnetic field, we see signatures of weak sign reversal as well. In all the plots as we move from blue to the green curve we increase the intervalley scattering strength α from below α_c to above α_c.

the intervalley scattering strength. The intervalley scattering strength depends on the magnitude and the type of the inherent disorder present in the material and the separation between the Weyl cones. Tuning the disorder in a material is rather complex; however, the separation between the Weyl cones may be tuned experimentally in some cases. For instance, in a Dirac semimetal (which turns into a Weyl semimetal in the presence of an external magnetic field), the separation between the Weyl cones is typically a function of the strength of the applied magnetic field [11,36,37]. Thus, the intervalley scattering strength can be tuned in a Dirac semimetal as a function of the applied magnetic field, resulting in the realization of the strong sign-reversed state. By fitting the magnetoconductivity data in Eq. (3) and extracting the parameters B_0, $\sigma_{zz}^{(0)}$, the phase plots in Fig. 3 can probed experimentally in a Dirac semimetal.

C. Planar Hall conductivity

Having discussed the longitudinal magnetoconductivity, here we wish to study the planar Hall conductivity. The dependence of the planar Hall conductivity σ_{xz} on the magnetic field is typically quadratic and we may expand it as [14]

$$\sigma_{xz}(B) = \sigma_{xz}^{(2)}(B - B_0)^2 + \sigma_{xz}^{(0)}, \tag{4}$$

where B_0 is vertex of the parabola, and $\sigma_{xz}^{(2)}$ is the quadratic coefficient. The planar Hall conductivity depends on the angle of the applied magnetic field, specifically as $\sin(2\gamma)$, where γ is the angle of the magnetic field with respect to the x axis [14] (see Fig. 1). To disentangle the effect of strain, we first evaluate the planar Hall conductivity in the absence of an external magnetic field. In Fig. 5(a) we plot the planar Hall conductivity $\sigma_{xz}(B_5)$ that is evaluated in the absence of external magnetic field for several different values of the intervalley scattering strength. The angular behavior with respect to γ_5 also turns out to be $\sin(2\gamma_5)$ as the case with the usual planar Hall conductivity. We also explicitly examine the effect of intervalley scattering α in Fig. 5(b). Even though the conductivity is expected to decrease with increasing scattering, the functional form has still never been explicitly evaluated, especially when the scattering is momentum dependent. Based on our numerics, we conclude find that the planar Hall conductivity induced by the chiral gauge field depends inversely on the scattering strength, i.e., $\sigma_{xz}(B_5) \sim 1/\alpha$.

1. *Opposing effects of external and chiral magnetic field*

Based on the above observations, one may naively conclude that the effect of the strain-induced chiral gauge field and the external magnetic field are precisely the same, as also concluded in Ref. [30]. We reexamine this conclusion by comparing and contrasting the behavior of the planar Hall conductivity when (i) external magnetic field is applied and the strain-induced field is absent, and (ii) when strain-induced field is present but external magnetic field is absent. We find the contribution to the planar Hall conductivity to be different both in sign and magnitude, which is in contrast to earlier claims [30]. Specifically, choosing $\gamma = \gamma_5$, we find that $\sigma_{xz}(B)$ when $B_5 = 0$ has the opposite sign and magnitude to the case $\sigma_{xz}(B_5)$ when $B = 0$. In other words, the effect of strain is to oppose the planar Hall effect with a different magnitude. Due to the difference in magnitude, the two effects do not cancel out each other. This feature has been highlighted in Fig. 6(a). We attribute this behavior to the inclusion of intervalley scattering, momentum dependence, as well as charge conservation that have been neglected in earlier works.

2. *Unusual conductivity*

Next, we study the planar Hall conductivity in the presence of both the external magnetic field and strain-induced chiral magnetic field. In the presence of an external magnetic field, the effect of strain is to shift and tilt the conductivity parabola, thereby resulting in weak sign reversal of the conductivity as shown in Fig. 6(b). In contrast to the longitudinal magneto-

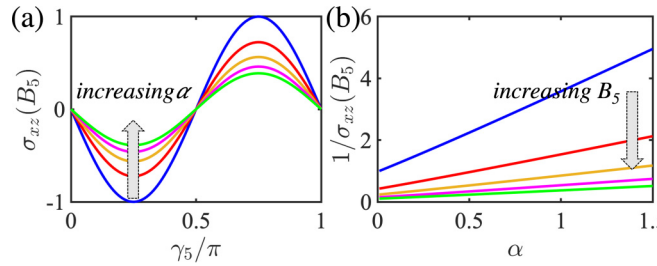

FIG. 5. Planar Hall conductivity for a minimal model of untilted TR broken WSM in the absence of any magnetic field. (a) Variation with respect to the angle γ_5. Increasing α reduces the conductivity, as expected. (b) PHC behaves as the inverse of scattering strength. Since $\sigma_{xz}(B_5 = 0) = 0$, we have normalized σ_{xz} appropriately in both the plots. In creasing B_5 field increases the conductivity.

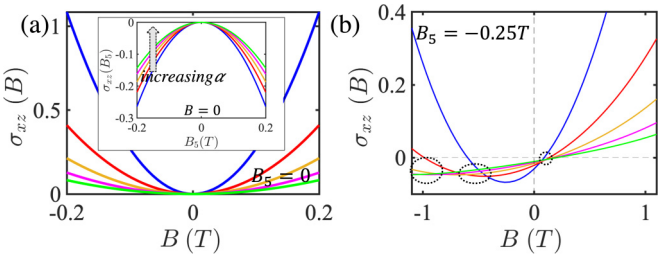

FIG. 6. Planar Hall conductivity for a minimal model of untilted TR broken WSM. (a) PHC as a function of external magnetic field B and no strain-induced field ($B_5 = 0$) is compared with the inset where PHC has been plotted as a function of B_5 with no external field ($B = 0$). The angle γ was chosen to be equal to γ_5. Strain opposes the planar Hall effect albeit with different magnitude. (b) PHC in the presence of both magnetic field and strain. The chiral gauge field causes weak sign reversal. The dotted ellipses highlight regions that show an anomalous behavior with respect to intervalley scattering strength. The width of lines is reduced for better visibility. In all the curves, as we go from blue to green, we increase α. All the plots are appropriately normalized.

conductivity, PHC never shows strong sign reversal even on increasing the intervalley scattering above the critical value. However, interestingly, we find that in a certain window of the magnetic field, increasing intervalley scattering strength increases the magnitude of the planar Hall conductivity, which is counterintuitive. We understand this behavior as the result of the opposing effects of strain-induced PHC and magnetic field-induced PHC. We better visualize this in Fig. 7, where we plot the planar Hall conductivity as a function of the intervalley scattering strength α. First, we notice that in the absence of B_5 field, the Hall conductivity shows some amount of nonlinearity as a function of $1/\alpha$. This is contrasted to Fig. 5(b) (the case when $B = 0$, $B_5 \neq 0$), where linear behavior was observed for all ranges of α. Second, in the presence of B_5 field, the behavior of σ_{xz} with respect to α can be strikingly different. Due to the weak sign reversal, σ_{xz} can switch signs, which explains the divergences in the plot in Fig. 7(b). Furthermore, we note that when σ_{xz} switches sign from positive to negative, the behavior with respect to α becomes anomalous, i.e., increasing α, increases the magnitude of σ_{xz}. This anomalous behavior with respect to the intervalley scattering strength is not observed for longitudinal magnetoconductivity.

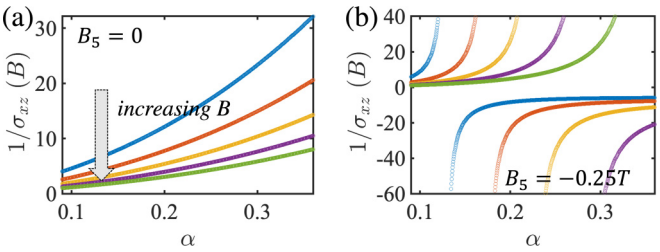

FIG. 7. Planar Hall conductance for a minimal model of untilted WSM as a function of intervalley scattering strength. (a) In absence of B_5 field. (b) In presence of B_5 field. In all the curves, as we go from blue to green, we increase B. All the plots are appropriately normalized.

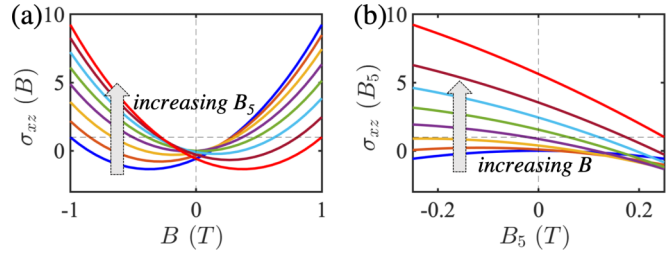

FIG. 8. Planar Hall conductance for a minimal model of untilted WSM. (a) As a function of the external B field. As we go from blue to red curve, we increase B_5 from -0.25 to $+0.25$ T. (b) As a function of the B_5 field. As we go from blue to red curve, we increase B from 0 to 1 T. All the plots are appropriately normalized. We chose $\gamma = \gamma_5 = 0.45\pi$, and $\alpha = 0.5$.

3. *Experimental implications*

Experimentally, in Dirac semimetals, where varying the external magnetic field may vary the intervalley scattering strength, one can may the behavior of σ_{xz} as a function of the intervalley scatteting strength, as shown in Fig. 7. Furthermore, one can also externally tune in the amount of strain and the magnitude of the external magnetic field that results in modulation the planar Hall conductivity σ_{xz} as shown in Fig. 8. Importantly, we expect σ_{xz} as a function of B to exhibit weak sign reversal while σ_{xz} as a function of B_5 to show strong sign reversal. This behavior can be again traced back to the opposing effects of magnetic field and strain discussed earlier.

III. TIME-REVERSAL BROKEN WSM WITH TILT

Having discussed the physics of strain-induced gauge field in a minimal untilted model of Weyl fermions, we now discuss the case when there is a finite tilt in the Weyl cones. The Hamiltonian is given by

$$H = \sum_{\chi} \sum_{\mathbf{k}} \chi \hbar v_F \left(\mathbf{k} \cdot \boldsymbol{\sigma} + t_z^{\chi} k_z\right). \tag{5}$$

Here t_z is the tilting parameter along the z axis. We only focus on the case when $t_z^{\chi} < v_F$, thus restricting ourselves to type-I Weyl semimetals.

A. Longitudinal magnetoconductivity

Depending on whether the two cones are tilted along the same or opposite direction, the behavior of both LMC and PHC can behave differently. In the absence of strain, if the cones are tilted in opposite directions, i.e., $t_z^{\chi} = -t_z^{\chi'}$, a linear in magnetic field term is added to the overall longitudinal magnetoconductivity, and the magnetoconductivity parabola is shifted and tilted along a particular direction. In other words, we can say that in the absence of external strain, tilting results in weak sign reversal, although this has never been explicitly pointed out in earlier works [34,38,39]. When the intervalley scattering strength is large, tilting the Weyl cones results in both weak and strong sign reversal.

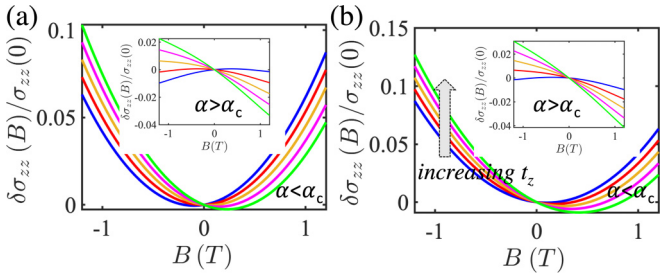

FIG. 9. LMC for a tilted TR broken WSM [Eq. (5)] with $t_z^1 = -t_z^{(-1)}$. (a) When $B_5 = 0.1$ T. (b) When $B_5 = -0.1$ T. The inset in both figures is for the case when $\alpha = 1.2 > \alpha_c$, while in the main figures $\alpha = 0.2 < \alpha_c$. As we move from blue to the green curve in both the plots, we increase t_z/v_F from 0 to 0.06. The opposing effects and adding effects of strain and tilt are highlighted in (a) and (b), respectively.

1. Oppositely tilted Weyl cones

In the presence of both tilt and strain, we arrive at a very interesting scenario. Both of these parameters, i.e., t_z and B_5, can tilt the LMC parabola either in the same direction or opposite direction, and this depends on the angle between the tilt direction and the strain-induced gauge field. In Fig. 9 we plot the longitudinal magnetoconductivity for a tilted TR broken WSM presented in Eq. (5) when the Weyl cones are tilted opposite to each other. Depending on the direction of the strain-induced gauge field B_5, the effects of tilting and strain can either add up or even cancel out. In Fig. 9(a), $B_5 > 0$, and the strain and tilting effects work in opposite directions, while in Fig. 9(b), $B_5 < 0$, and the strain and tilting effects work in the same direction. The tilting of the parabola is due to the addition of a linear-in-B component in the overall magnetoconductivity. Their signs may or may not be equal to each other depending on the relative orientation between tilt and strain. The plots imply weak sign reversal for $\alpha < \alpha_c$, and additionally, strong sign reversal for $\alpha > \alpha_c$. In Fig. 10(a) we plot the quadratic coefficient $\sigma_{zz}^{(2)}$ as a function of both tilt and intervalley scattering strength in the presence of a B_5 field. We note that the presence of the tilt parameter curves the contour α_c separating the two strong sign-reversed regions, i.e., $\alpha_c = \alpha_c(t_z)$. This dependence is expected because the presence of tilt parameter contributes additionally to the dissimilarity of the Fermi surfaces.

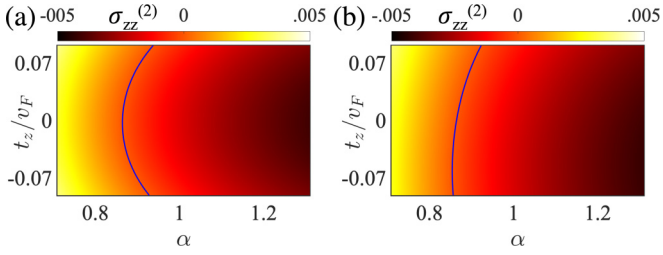

FIG. 10. (a) The quadratic coefficient of the longitudinal magnetoconductivity $\sigma_{zz}^{(2)}$ for tilted TR broken WSM. (a) $t_z^{(1)} = -t_z^{(-1)}$. (b) $t_z^{(1)} = t_z^{(-1)}$. Strain-induced chiral magnetic field was fixed to $B_5 = 0.1$ T in both the cases. The blue contour separates the regions when $\sigma_{zz}^{(2)} > 0$ and when $\sigma_{zz}^{(2)} < 0$ (strong sign reversal).

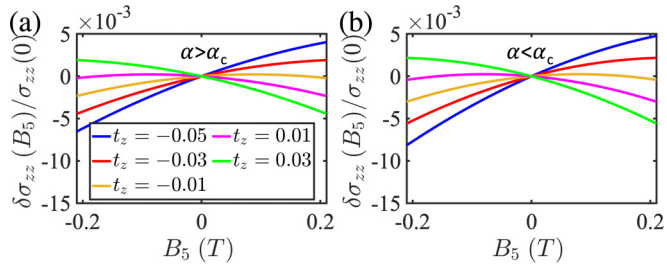

FIG. 11. LMC for a tilted TR broken WSM when the tilts are oriented in the same direction. Both weak and strong sign reversal is observed irrespective of the intervalley scattering strength. The legends are same in both the plots.

2. Weyl cones tilted in the same direction

In the absence of strain it is known that when the nodes are oriented along the same direction ($t_z^1 = t_z^{-1}$), the linear component of the longitudinal magnetoconductivity does not survive as the contributions from both nodes cancel out [34,38,39]. Hence, as expected, only strong sign reversal is observed as a function of intervalley scattering strength. Now, in the presence of only strain-induced field, such cancellation does not occur and one observes weak sign reversal as a function of the tilt parameter. Furthermore, in the presence of B_5 field and absence of external magnetic field, we observe both strong and weak sign reversal. To illustrate this, in Fig. 11 we plot LMC for a tilted TR broken WSM when the tilts are oriented in the same direction. When both magnetic field and strain-induced chiral magnetic field are present, the combination of two can give rise to interesting features. In Fig. 10(b) we plot the quadratic coefficient $\sigma_{zz}^{(2)}$ as a function of both tilt and intervalley scattering strength in the presence of a B_5 field. The $\alpha_c(t_z)$ curve separating the two sign-reversed phases is different depending on the fact whether the Weyl cones are oriented opposite to each other or oriented along the same direction.

3. Striking phase plots

Striking features are observed for the parameters B_0 (the vertex of the parabola) as well as $\sigma_{zz}^{(0)}$. We demonstrate this in Fig. 12. We fix strain-induced gauge field to be around $B_5 = 0.1$ T. Let us first focus on the case when the Weyl cones are oriented opposite to each other. When $\alpha < \alpha_c$, the sign of B_0 changes continuously from negative to positive as t_z is varied from negative to positive. On the other hand, when $\alpha > \alpha_c$, the sign of B_0 changes from positive to negative as t_z is varied from negative to positive. The effects of strain and tilt and strain can either add up or cancel out and the combination can tilt the parabola overall to the left or to the right resulting in weak sign reversal. This is demonstrated in the color plot in Fig. 12(a). When $\alpha > \alpha_c$, the sign of B_0 changes discontinuously (feature of strong sign reversal). Now, since weak sign reversal does not change the sign of $\sigma^{(0)}$, we do not see a sign change in $\sigma^{(0)}$ as one varies the tilt for a given value of α. The sign change in $\sigma^{(0)}$ only occurs as a result of strong sign reversal [Fig. 12(b)]. Now, when the cones are oriented along the same direction, the linear component arising from the tilt is canceled out and hence we do not observe any change in B_0

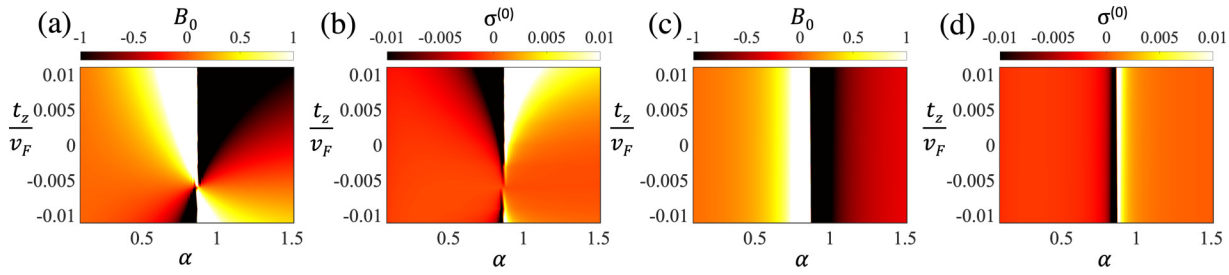

FIG. 12. LMC parameters for tilted TR broken WSMs. The center of the parabola B_0 (a) and $\sigma^{(0)}$ as a function of the tilt parameter and intervalley scattering strength, in the presence of a fixed value of chiral gauge magnetic field $B_5 = 0.1T$. The tilts are oriented opposite to each other in plots (a) and (b). The plots (c) and (d) are for the case when the Weyl cone tilts are oriented in the same direction.

or $\sigma^{(0)}$ by varying the tilt. The only change occurs at $\alpha = \alpha_c$ due to strong sign reversal. This is highlighted in Figs. 12(c) and 12(d).

B. Planar Hall effect

Next we discuss the strain-induced planar Hall effect for tilted TR broken Weyl semimetals. When the cones are oriented along the opposite directions we observe a $\sim \sin 2\gamma_5$ behavior and the effect of the tilt is only quantitative, and so is the effect of varying intervalley scattering strength. On the other hand, when the cones are oriented along the same direction, the behavior changes to $\sim \sin \gamma_5$. Changing the tilt parameter can switch the sign of the planar Hall conductance as well. We demonstrate these features in Fig. 13. Varying the intervalley scattering strength only changes the overall magnitude (not explicitly plotted).

Finally, we discuss the behavior of conductivity on changing the intervalley scattering strength α. In Fig. 14, we plot the change in the magnitude of the planar Hall conductivity $[|\sigma_{xz}(\alpha)| - |\sigma_{xz}(\alpha + \epsilon)|]$ for an infinitesimal increase in the scattering strength (by a small amount ϵ). In both cases, i.e., when the Weyl cones tilted in opposite direction, and when the Weyl cones are tilted in the same direction, we find regions in the $B_5 - t_z$ space where anomalous behavior of the Hall conductivity is observed, i.e., the magnitude of conductivity increases on increasing the intervalley scattering strength. We have already seen this behavior for untilted WSM as well (Fig. 7), and here we calculate its dependence on the tilting of the Weyl cones. Before closing this section, we point out that in experiments where strain can be applied and manipulated on the inhomogeneous samples can test the above predictions.

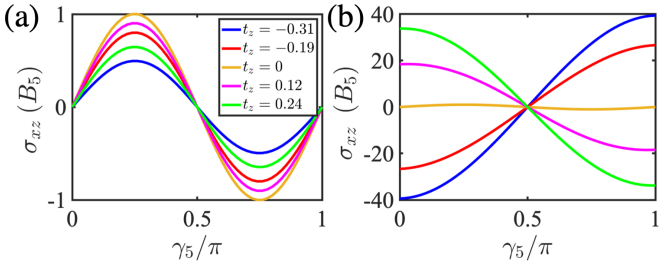

FIG. 13. (a) The planar Hall conductance in TR broken tilted WSM as a function of the angle γ_5 when (a) the cones are tilted along opposite direction, and (b) cones are oriented along the same direction. The legends are the same in both the plots. Both plots are appropriately normalized such that the yellow curve is identical in both the figures as expected.

IV. INVERSION ASYMMETRIC WEYL SEMIMETALS

Having discussed the effect of strain in time-reversal broken WSMs we now move on to the case of inversion asymmetric WSMs. To this end, we will restrict our attention to the following minimal model for an inversion asymmetric WSM that consists of four nodes as dictated by symmetry considerations:

$$H = \sum_{n=1}^{4} \left(\chi_n \hbar v_F \mathbf{k} \cdot \boldsymbol{\sigma} + \hbar v_F t_z^n k_z \sigma_0\right). \tag{6}$$

The system consists of four Weyl nodes located at the points $\mathbf{K} = (\pm k_0, 0, \pm k_0)$ in the Brillouin zone. In Eq. (6), χ_n is the chirality, and we are also introducing the parameter t_z^n, that represents the tilting of the Weyl cone. The Weyl cones are assumed to be tilted only along the z direction. Specifically, $(1, t_z) = (\chi_1, t_z^{(1)}) = (-\chi_2, t_z^{(2)}) = (\chi_3, -t_z^{(3)}) = (-\chi_4, -t_z^{(4)})$, such that inversion symmetry is broken. The tilt parameter t_z is considered to be less than unity. Figure 15(a) plots the schematic diagram of this prototype inversion asymmetric Weyl semimetal. Specifically, we must consider four intranode scattering channels (node $n \Longleftrightarrow n$) and four internode scattering channels (node $n \Longleftrightarrow [n+1] \bmod 4$). The

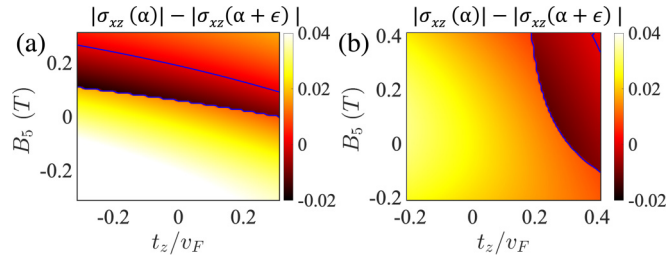

FIG. 14. Change in the magnitude of the planar Hall conductivity $[|\sigma_{xz}(\alpha)| - |\sigma_{xz}(\alpha + \epsilon)|]$ for a tilted TR broken WSM [Eq. (5)] on infinitesimally increasing in the scattering strength (by ϵ). (a) The Weyl cones are tilted in opposite direction. (b) The Weyl cones are tilted in the same direction. In the region enclosed within blue contours, we find anomalous behavior of conductivity with the scattering strength, i.e., the magnitude of the conductivity increases on the increase of scattering strength. We choose $\alpha = 0.5$ and $\epsilon = 0.01$.

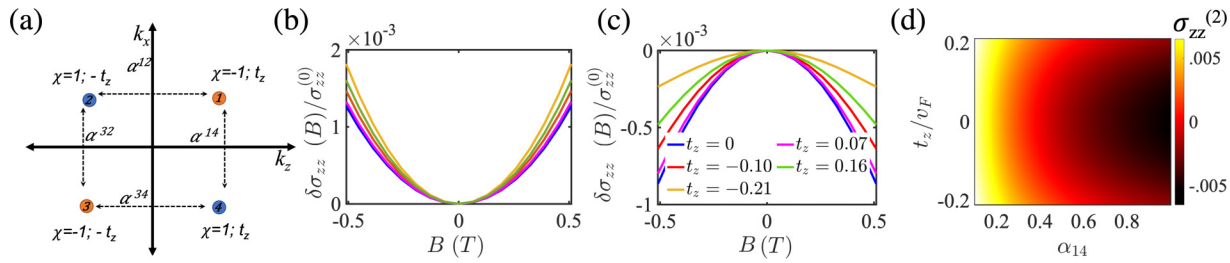

FIG. 15. (a) Schematic of Weyl nodes in a prototype model of an inversion asymmetric Weyl semimetal. Here χ is the chirality, t_z is the tilt, and α^{ij} are scattering rates from node i to node j. (b) LMC as a function of magnetic field when the intervalley scattering rates are less than the critical value. (c) LMC as a function of magnetic field when the intervalley scattering rates are above the critical value. The legends in (b) and (c) are identical. (d) $\sigma_{zz}^{(2)}$ for a fixed value of $\alpha_{12} = 0.19$. Plots (b), (c), and (d) are in the absence of strain, i.e., $B_5 = 0$.

dimensionless scattering strength between node m and node n is denoted as α^{mn}. For simplicity, we ignore the scattering between nodes (4 $\longleftrightarrow$ 2) and nodes (1 $\longleftrightarrow$ 3) since they involve a large momentum transfer compared to others. The four internode scatterings can be divided into two categories: (i) scattering between Weyl cones of opposite chirality and opposite tilt orientation (1 $\longleftrightarrow$ 2) and (3 $\longleftrightarrow$ 4), and (ii) scattering between Weyl cones of opposite chirality and same tilt orientation (1 $\longleftrightarrow$ 4) and (2 $\longleftrightarrow$ 3). Since both these categories result in different behaviors, it is of interest to see the interplay between the two.

A. LMC in the absence of strain

We first examine the behavior of longitudinal magnetoconductivity in the absence of any strain. Earlier, we examined that for a system of only two tilted cones (of opposite chirality), weak sign reversal is possible only if the cones are oriented opposite to each other. However, in the current case, weak sign reversal generated by internode scattering channel (1 $\longleftrightarrow$ 2) is exactly canceled by scattering channel (4 $\longleftrightarrow$ 3). Second, the scatterings (1 $\longleftrightarrow$ 4) and (2 $\longleftrightarrow$ 3) do not cause weak sign reversal as they involve Weyl cones with the same tilt. Therefore, in the absence of B_5 field, weak sign reversal is not observed for the case of an inversion asymmetric WSM. In Fig. 15 we plot longitudinal magnetoconductivity for the inversion asymmetric Weyl semimetal [Eq. (6)] in the absence of strain-induced chiral gauge field B_5. As discussed, we do not observe any signature of weak sign reversal, and there is only strong sign reversal when α_{12} and/or α_{14} are large enough. Increasing tilt does not qualitatively change the behavior and increasing the magnitude of the tilt in either direction is only seen to increase the magnitude of magnetoconductivity.

B. LMC in the presence of strain and absence of external magnetic field

Next, we study the behavior in the absence of an external magnetic field but in the presence of strain-induced gauge field B_5. First, similar to the case with TR broken Weyl semimetals, we find that strain-induced chiral magnetic field B_5 always results in a negative LMC coefficient $\sigma_{zz}^{(2)}$. This results in contradiction to earlier claims that find an increase in longitudinal magnetoconductivity with strain [28,30]. The reason can be traced out to the noninclusion of intervalley scattering, momentum-dependent scattering, and charge conservation, all of which are included in this work (see the Appendix). Furthermore, we find that strain, by itself, results in strong sign reversal, while tilting, additionally, results in weak sign reversal. In Fig. 16(a) we plot LMC as a function of strain-induced magnetic field B_5, which clearly demonstrates these features. As before, we fit the magnetoconductivity via the following expression:

$$\sigma_{zz}(B_5) = \sigma_{zz}^{(2)}(B - B_{50})^2 + \sigma_{zz}(B_{50}), \tag{7}$$

where the slope of the conductivity $\sigma_{zz}^{(2)}$ is always found to be negative irrespective of the value of tilt, strain, intervalley scattering strengths across either nodes. The center of the parabola (B_{50}) directly correlates with the tilt parameter t_z. Depending on the sign of t_z, B_{50} can be either positive or negative. The parameter B_{50} is also found to have dependence on the scattering strength, but this dependence is relatively weak compared to the dependence on t_z. In Figs. 16(b)–16(d), we plot the parameters $\sigma_{zz}^{(2)}$, B_{50}, and $\sigma_{zz}(B_{50})$ as a function of α_{14},

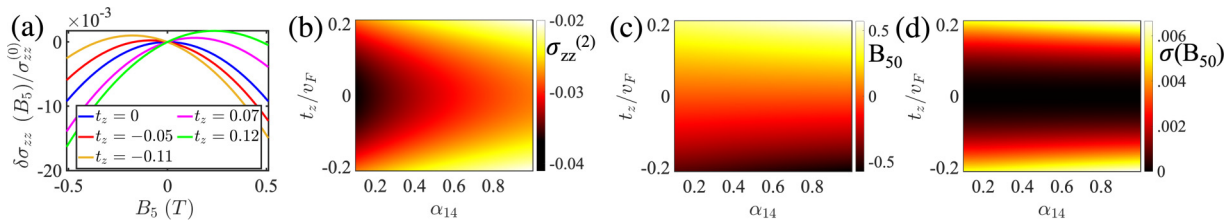

FIG. 16. LMC for inversion asymmetric Weyl semimetal in the presence of strain-induced chiral magnetic field (B_5) and absence of magnetic field. (a) A finite tilt can result in weak sign reversal. The plot is for a fixed value of $\alpha_{12} = 0.4$, but the qualitative behavior is independent of scattering strength. (b), (c), and (d) plot the parameters $\sigma_{zz}^{(2)}$, B_{50}, and $\sigma(B_{50})$ as a function of parameters α_{14} and t_z. We fixed $\alpha_{12} = 0.19$.

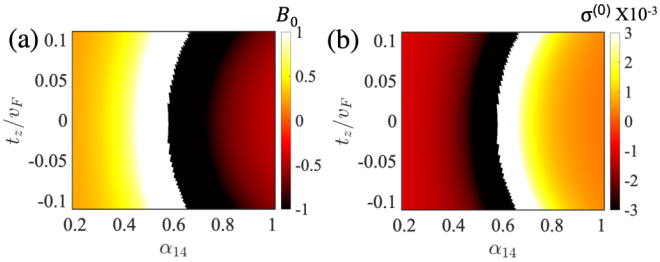

FIG. 17. The parameters B_0 (a) and $\sigma^{(0)}$ (b) for inversion asymmetric Weyl semimetals [Eq. (6)] in the presence of both strain-induced field and external magnetic field. We have fixed $\alpha_{12} = 0.3$, $B_5 = 0.1$ T. Weak sign reversal is not observed and strong sign-reversal occurs at $\alpha_{14} = \alpha_{14c}(t_z)$.

and t_z, keeping α_{12} fixed, and $B = 0$. No sharp discontinuities are observed in the parameters since the system is already in strong sign-reversed state.

C. LMC in the presence of both strain and external magnetic field

In inversion asymmetric inhomogeneous Weyl semimetals, interesting effects can occur as a result of the interplay between the strain-induced chiral gauge field, external magnetic field, and the tilt parameter, as demonstrated in Fig. 17. We examine LMC as a function of external magnetic field for a fixed value of chiral gauge field, and use Eq. (3) to evaluate the fit parameters B_0, $\sigma_{zz}^{(2)}$, and $\sigma_{zz}^{(0)}$. We do not find a signature weak sign reversal, and only strong sign reversal occurs when the intervalley scattering $\alpha_{14} > \alpha_{14c}$, where α_{14c} now is a function of tilt parameter. Around $\alpha = \alpha_{14c}(t_z)$ we find a sharp change in the sign of the parameters B_0 and $\sigma_{zz}^{(0)}$ that corresponds to a continuous change of sign in $\sigma_{zz}^{(2)}$ as well.

D. Experimental implications

It is worthwhile pointing out that by identifying the parameters B_0 and $\sigma_{zz}^{(0)}$ from the experimentally measured conductivity, their signs may help identify the dominant scattering mechanisms in the system, i.e., either internode or intranode scattering, and also provide us insight about the strain in the samples as well as the tilting if the Weyl cones. Experimentally, one may also study LMC in inversion asymmetric Weyl semimetals by tuning the amount of strain in the system. Therefore, it is of interest to study the effect of varying strain on LMC. In Fig. 18(a) we plot $\delta\sigma_{zz} = \sigma_{zz}(B) - \sigma_{zz}(B = 0)$ simultaneously varying the intervalley scattering strength α_{14} as well as the strain-induced chiral gauge field B_5. We see signatures of both weak and strong sign reversal. Increasing α beyond α_c results in strong sign reversal, while change in the tilt parameter results in weak sign reversal. We fix the value of α_{12}, and evaluate the fit parameters of $\sigma_{zz}(B)$ from Eq. (3). Figure 18(b) plots $\sigma_{zz}^{(2)}$ as a function of B_5 and α_{14}. The contour α_{14c} where $\sigma_{zz}^{(2)}$ switches sign shows a dependence on B_5 as well. Therefore, the contour α_c is in general a function of both t_z and B_5. Figures 18(c) and 18(d) plot the parameters B_0 and $\sigma_{zz}^{(0)}$ obtained from Eq. (3), both of which display very interesting behavior as a result of varying B_5 and α_{14}. In Fig. 18(c), when $\alpha < \alpha_c(B_5)$, the sign of B_0 changes from negative to positive as B_5 changes sign from negative to positive. When $\alpha > \alpha_c(B_5)$, the change of sign is from positive to negative. At $\alpha = \alpha_c(B_5)$, there is strong sign reversal resulting in sharp contrasting features on the both sides of $\alpha_c(B_5)$. On the other hand, in Fig. 18(d), $\sigma_{zz}^{(0)}$ does not change sign as B_5 changes sign, but like B_0, it displays striking behavior around $\alpha_c(B_5)$ due to strong sign reversal.

E. Planar Hall effect

Before closing this section, we also comment on the planar Hall effect in inversion asymmetric Weyl semimetals. Figure 19(a) plots the planar Hall conductivity σ_{xz} as a function of the angle γ_5 in the absence of an external magnetic field and presence of strain-induced gauge field B_5. The PHC behaves as $\sim \sin(2\gamma_5)$ as in Fig. 13(a). The contribution from the two time-reversed and opposite tilt Weyl node pairs adds up, while the contribution from two time-reversed and same tilt Weyl node pairs cancels out, and that is why we do not get a $\sim \sin(\gamma_5)$ trend as in Fig. 13(b). In Figure 19(b), we plot the change in the magnitude of the planar Hall conductivity upon infinitesimally increasing the intervalley strength α_{14}. We again notice a region in the $B_5 - t_z$ space where the variation of conductivity is anomalous, i.e., increasing intervalley scattering increases the magnitude of the conductivity. A similar plot is observed when we instead fix α_{14} and vary α_{12}, therefore, we do not explicitly plot this here.

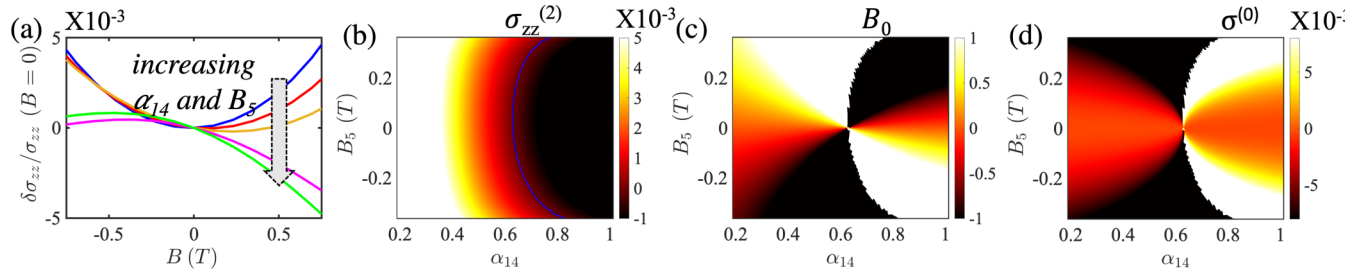

FIG. 18. (a) LMC for inversion asymmetric Weyl semimetal. As we move from the blue to the green curve, we simultaneously increase B_5 as well as α_{14}. Both weak and strong sign-reversal are exhibited. The plots (b), (c), and (d) plot the parameters $\delta\sigma_{zz}^{(2)}$, B_0, and $\sigma^{(0)}$ for fixed α_{12} and $t_z \neq 0$. The blue contour in plot (b) separates the phases where $\sigma_{zz}^{(2)}$ changes sign. Again, we see signatures of both weak and strong sign-reversal. The tilt parameter is fixed to $t_z/v_F = -0.1$.

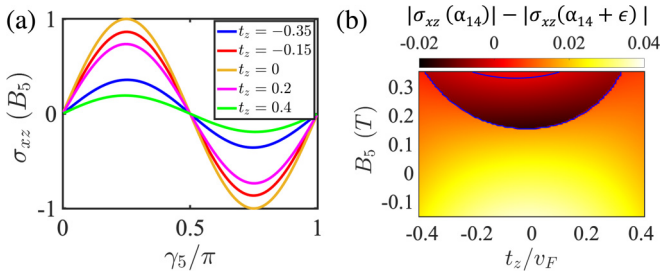

FIG. 19. Planar Hall conductance for inversion asymmetric Weyl semimetal. (a) PHC as a function of γ_5, when $B = 0$ and $B_5 \neq 0$. (b) The change in the magnitude of the planar Hall conductivity on increasing α_{14} infinitesimally. In the region between the blue contours, we observe anomalous increase in conductivity. Here we fix, $B = 1$ T, $\alpha_{12} = 0.4$, $\alpha_{14} = 0.5$, and $\epsilon = 0.01$.

V. EFFECT OF INHOMOGENEOUS B_5 FIELD

So far we have assumed that the system is under a strain profile that gives a constant pseudomagnetic field, i.e., the $\mathbf{B}_5^{\chi}$ field is position independent. A spatially modulating chiral magnetic field would stem from an appropriate modulation of the valley-dependent vector potential in momentum space $\mathbf{A}^{\chi}$. We anticipate that the effect of including the higher-order terms in the Fourier expansion could result in the following effects: (i) averaging of the behavior when the sample size is larger than regions where B_5 might be considered homogeneous, (ii) the low-energy Weyl Hamiltonian may acquire additional higher-order terms that may result in very interesting effects. We reserve the problem of finding Boltzmann solutions to an inhomogeneous magnetic field for the future. Keeping only the leading-order term in the Fourier series expansion of $\mathbf{A}^{\chi}$ about $k = 0$, we end up with the conclusion that the original Hamiltonian now has an additional term that is linear in k. Here, we content ourselves with incorporating this effect into the modulation of the Fermi velocity [40–42], such that $v_F \longrightarrow v_F + \chi\delta v_F$, where δ is a dimensionless parameter that incorporates the change in Fermi velocity. To this end, we study the effect of inhomogeneous strain-induced chiral gauge field B_5 on TR broken untitled WSM and inversion asymmetric Weyl semimetal.

A. TR broken untilted WSM under inhomogeneous strain

In Fig. 20 we plot the LMC as a function of B in presence of inhomogeneous B_5 field. We observe that inhomogeneity causes deviations from the quadratic dependence of LMC on the magnetic field and also can lead to nonmonotonic behavior. We also have studied the effect of inhomogeneous B_5 field on LMC for the following cases: (i) $B_5 = 0$ and $B \neq 0$, (ii) $B_5 \neq 0$ and $B = 0$. In case (i), we find that the LMC becomes positive at large enough δ for all values of α. In case (ii), no sign reversal is observed but inhomogeneity in B_5 shifts the focus of the parabola. We do not explicitly plot this behavior. We conclude that weak inhomogeneity in the strain-induced chiral gauge field results primarily in quantitative changes while moderate amount of inhomogeneity may result in nonmonotonic behavior of LMC.

B. Inversion asymmetric tilted WSM under inhomogeneous strain

We consider the four-node minimal model of inversion asymmetric tilted WSM as described in Eq. (6). To study the effect of inhomogeneity in the strain-induced chiral magnetic field B_5, we modify the Fermi velocity at each valley as described in the case of TR broken untilted WSMs. In Figs. 21(a)–21(d) we have plotted the change in LMC, i.e., $\delta\sigma_{zz}(B)$ vs B for different values of δ. As in the case of homogeneous B_5 field, we are able fit the magnetoconductivity via $\sigma_{zz}(B_5) = \sigma_{zz}^{(2)}(B - B_{50})^2 + \sigma_{zz}(B_{50})$. As described earlier, due to the nonzero B_5 field the LMC parabola has a different vertex and shows "weak sign reversal." The effect of the inhomogeneity is to shift the vertex and focus of the LMC parabola. We also have studied the LMC as a function of the B_5 field in the absence of an external magnetic field at different values of tilt t_z. We find that weak sign reversal is intact up to $\delta = 0.20$. We do not plot this explicitly. We conclude that weak inhomogeneity in the chiral gauge field does not result in qualitative changes of the results.

VI. CONCLUSIONS

The sign of longitudinal magnetoconductivity in Weyl semimetals due to chiral anomaly has been a subject of intense research [31–34,38,39,43–50]. Almost unanimously, the sign of longitudinal magnetoconductivity has been agreed upon to be positive, at least within the limit of weak magnetic fields. However, various factors, such as tilting of the Weyl cones, strain, and inhomogeneities in the material, qualitatively affect the LMC in Weyl semimetals. The interplay between

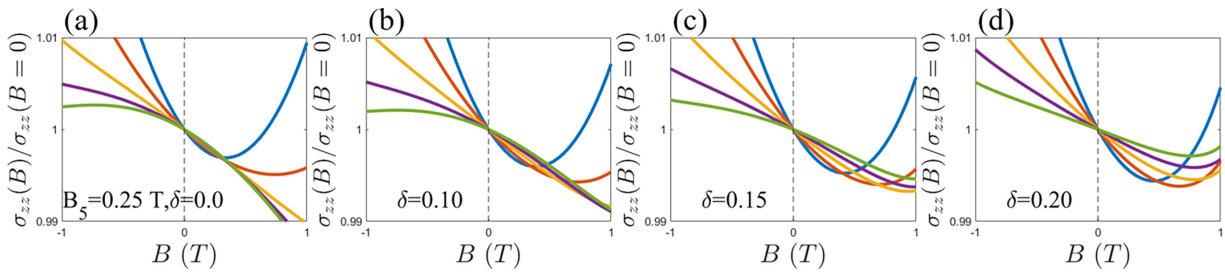

FIG. 20. LMC vs B for minimal model of TR broken untilted WSM for an inhomogeneous B_5 field for different values of δ. By changing the δ we can tune the Fermi velocity at each valley. In all the plots, as we go from blue to green curve, we increase the strength of the intervalley scattering α. We have also fixed the chiral magnetic field $B_5 = 0.25$ T. Here δ is a dimensionless parameter accounting for the change in the Fermi velocity due to the presence of inhomogeneous B_5 field.

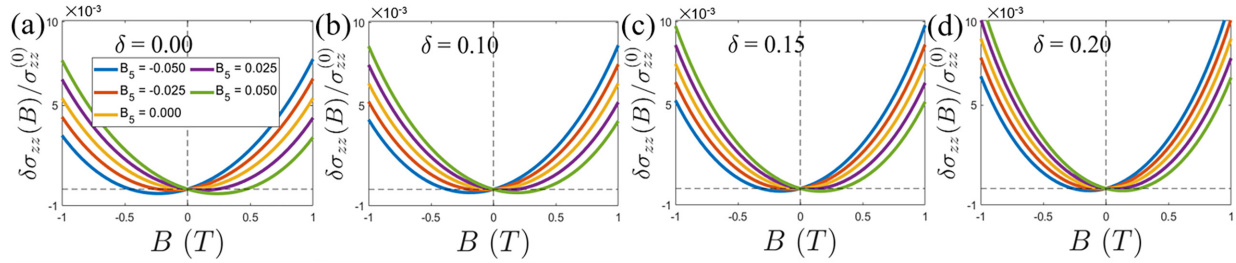

FIG. 21. LMC for inversion asymmetric tilted WSM for inhomogeneous strain-induced chiral magnetic field (B_5). As we move from blue to green curve we vary the value of B_5 from -0.05 to 0.05 T. In all the plots we have fixed the value of $\alpha_{12} = 0.30$, $\alpha_{14} = 0.31$, and $t_z/v_F = -0.1$. The chirality of all four nodes is chosen in such a way that the inversion symmetry is broken. Here $v_F^{(i)} \longrightarrow v_F^{(i)} + \delta\chi^{(i)}v_F^{(i)}$, $\chi^{(i)} = (-1)^i$ with $i = 1, 2, 3, 4$ and $\delta > 0$. Here δ is a dimensionless parameter accounting for the change in the Fermi velocity due to the presence of inhomogeneous B_5 field.

various parameters, such as intervalley scattering, tilt, strain-induced chiral gauge field, and the external magnetic field, leads to many striking features in both the longitudinal magnetoconductance and the planar Hall conductance of Weyl semimetals, which has been the focus of this work.

In this work, we first show the conventional method of assigning a sign to magnetoconductivity, i.e., comparing the magnitude of conductivity for field B with $B \pm \epsilon$ (ϵ being arbitrary), leads to ambiguities when the system is subjected to strain. Specifically, the sign of magnetoconductivity could depend on the direction of the magnetic field. Thus, there is a necessity to define weak sign reversal and strong sign reversal, both of which are qualitatively different and result in qualitatively different responses. Weak sign reversal, in general, leads to smooth changes in the fit parameters of the conductivity, while strong sign reversal leads to very sharp changes. Weak sign reversal is specifically characterized by a change in the vertex and the axis of the parabola of conductivity with respect to the magnetic field. In contrast, strong sign reversal is characterized by an opposite orientation, i.e., the direction in which the parabola opens is reversed. The qualitative difference between strong and weak sign reversal stems from the fact that unlike weak sign reversal, strong sign reversal (with respect to an external magnetic field) depends on the strength of intervalley scattering. Tables I and II highlight the differences as well.

Broadly speaking, (i) when strain-induced chiral gauge field is absent and external magnetic field is present, strong intervalley scattering results in strong sign reversal; (ii) when chiral gauge field is present and magnetic field is absent, the system, by default, shows strong sign-reversed state for both weak and strong intervalley scattering; (iii) when both chiral gauge and external magnetic field are present, there is both weak and strong sign reversal. The latter is also experimentally the most relevant scenario, and we show that it leads to very striking phase plots that can be explored experimentally in current and upcoming experiments in Weyl semimetals. In practice, the parameters could be evaluated by fitting the conductivity from the experiments, which could give us insight into the system's strain, tilt, and dominant scattering mechanism.

We have also studied the effect of strain on the planar Hall conductance. Another striking feature of anomalous variation of the planar Hall conductivity is also unraveled due to the rich interplay between the chiral gauge and external magnetic field, where the magnitude of conductivity can increase with increasing scattering strength. Last, we also briefly comment that the presence of weak inhomogeneities in the chiral gauge field only quantitatively affects the results. In this paper, we have restricted ourselves to the case where $k = 0$ term in the Fourier series expansion of $\mathbf{A}^\chi$ dominates over the others. We anticipate that the effect of including the higher-order terms in the Fourier expansion could result in the following effects: (i) averaging of the behavior when the sample size is larger than regions where B_5 might be considered homogeneous, (ii) the low-energy Weyl Hamiltonian may acquire additional higher-order terms that may result in very interesting effects. A full-fledged Boltzmann analysis for inhomogeneous fields remains an important study reserved for the future.

ACKNOWLEDGMENTS

A.A. acknowledges support from IIT Mandi HTRA. G.S. acknowledges support from SERB Grant No. SRG/2020/000134 and the IIT Mandi Seed Grant No. IITM/SG/GS/73. S.T. acknowledges support from Grant No. NSF 2014157, and ARO Grant No. W911NF22102. Discussions with S. Nandy are gratefully acknowledged.

APPENDIX: BOLTZMANN FORMALISM FOR MAGNETOTRANSPORT

Using the quasiclassical Boltzmann theory, we study transport in Weyl semimetals in the limit of weak electric and magnetic fields. Since quasiclassical Boltzmann theory is valid away from the nodal point such that $\mu^2 \gg \hbar v_F^2 eB$, therefore, without any loss of generality we will assume that the chemical potential lies in the conduction band. The phenomenological Boltzmann equation for the nonequilibrium distribution function $f_{\mathbf{k}}^\chi$ can be expressed as [51]

$$\left(\frac{\partial}{\partial t} + \dot{\mathbf{r}}^\chi \cdot \nabla_{\mathbf{r}} + \dot{\mathbf{k}}^\chi \cdot \nabla_{\mathbf{k}}\right) f_{\mathbf{k}}^\chi = \mathcal{I}_{\text{coll}}\left[f_{\mathbf{k}}^\chi\right], \tag{A1}$$

where the collision term on the right-hand side of the equation incorporates the effects of scattering due to impurities. In the presence of electric (**E**) and magnetic (**B**) fields, the

semiclassical dynamics of the Bloch electrons is [22]

$$\dot{\mathbf{r}}^{\chi} = \mathcal{D}^{\chi}\left[\frac{e}{\hbar}\left(\mathbf{E}\times\mathbf{\Omega}^{\chi} + \frac{e}{\hbar}(\mathbf{v}^{\chi}\cdot\mathbf{\Omega}^{\chi})\mathbf{B} + \mathbf{v}_{\mathbf{k}}^{\chi}\right)\right],$$
$$\dot{\mathbf{p}}^{\chi} = -e\mathcal{D}^{\chi}\left(\mathbf{E} + \mathbf{v}_{\mathbf{k}}^{\chi}\times\mathbf{B} + \frac{e}{\hbar}(\mathbf{E}\cdot\mathbf{B})\mathbf{\Omega}^{\chi}\right), \tag{A2}$$

where $\mathbf{v}_{\mathbf{k}}^{\chi}$ is the band velocity, $\mathbf{\Omega}^{\chi} = -\chi\mathbf{k}/2k^3$ is the Berry curvature, and $\mathcal{D}^{\chi} = (1 + e\mathbf{B}\cdot\mathbf{\Omega}^{\chi}/\hbar)^{-1}$. The self-rotation of Bloch wave packet also gives rise to an orbital magnetic moment (OMM) [35] $\mathbf{m}_{\mathbf{k}}^{\chi}$. In the presence of magnetic field, the OMM shifts the energy dispersion as $\epsilon_{\mathbf{k}}^{\chi} \to \epsilon_{\mathbf{k}}^{\chi} - \mathbf{m}_{\mathbf{k}}^{\chi}\cdot\mathbf{B}$. Interestingly, the Berry curvature and the orbital magnetic moment turn out to be independent of the tilting of the Weyl cones.

The collision integral must take into account scattering between the two Weyl nodes (internode, $\chi \Longleftrightarrow \chi'$), as well as scattering within a Weyl node (intranode, $\chi \Longleftrightarrow \chi$), and thus $\mathcal{I}_{\rm coll}[f_{\mathbf{k}}^{\chi}]$ can be expressed as

$$\mathcal{I}_{\rm coll}\left[f_{\mathbf{k}}^{\chi}\right] = \sum_{\chi'}\sum_{\mathbf{k}'} W_{\mathbf{k},\mathbf{k}'}^{\chi\chi'}\left(f_{\mathbf{k}'}^{\chi'} - f_{\mathbf{k}}^{\chi}\right), \tag{A3}$$

where the scattering rate $W_{\mathbf{k},\mathbf{k}'}^{\chi\chi'}$ is given by [51]

$$W_{\mathbf{k},\mathbf{k}'}^{\chi\chi'} = \frac{2\pi}{\hbar}\frac{n}{\mathcal{V}}\left|\langle\psi_{\mathbf{k}'}^{\chi'}|U_{\mathbf{k}\mathbf{k}'}^{\chi\chi'}|\psi_{\mathbf{k}}^{\chi}\rangle\right|^2\delta\left(\epsilon_{\mathbf{k}'}^{\chi'} - \epsilon_F\right). \tag{A4}$$

In the above expression n is the impurity concentration, $\mathcal{V}$ is the system volume, $|\psi_{\mathbf{k}}^{\chi}\rangle$ is the Weyl spinor wave function (which is obtained by diagonalizing the low-energy Weyl Hamiltonian given in the main text), $U_{\mathbf{k}\mathbf{k}'}^{\chi\chi'}$ is the scattering potential, and ϵ_F is the Fermi energy. The scattering potential profile $U_{\mathbf{k}\mathbf{k}'}^{\chi\chi'}$ is determined by the nature of impurities. Here we restrict ourselves to only nonmagnetic pointlike impurity, but distinguish between intervalley and intravalley scattering. This can be controlled independently in our formalism. Thus, the scattering matrix is momentum independent but has a dependence on the chirality, i.e., $U_{\mathbf{k}\mathbf{k}'}^{\chi\chi'} = U^{\chi\chi'}\mathbb{I}$.

The distribution function is assumed to take the form $f_{\mathbf{k}}^{\chi} = f_0^{\chi} + g_{\mathbf{k}}^{\chi}$, where f_0^{χ} is the equilibrium Fermi-Dirac distribution function and $g_{\mathbf{k}}^{\chi}$ indicates the deviation from equilibrium. In the steady state, the Boltzmann equation [Eq. (A1)] takes the form

$$\left[\left(\frac{\partial f_0^{\chi}}{\partial\epsilon_{\mathbf{k}}^{\chi}}\right)\mathbf{E}\cdot\left(\mathbf{v}_{\mathbf{k}}^{\chi} + \frac{e\mathbf{B}}{\hbar}\left(\mathbf{\Omega}^{\chi}\cdot\mathbf{v}_{\mathbf{k}}^{\chi}\right)\right)\right] = -\frac{1}{e\mathcal{D}^{\chi}}\sum_{\chi'}\sum_{\mathbf{k}'} W_{\mathbf{k}\mathbf{k}'}^{\chi\chi'}\left(g_{\mathbf{k}'}^{\chi} - g_{\mathbf{k}}^{\chi}\right). \tag{A5}$$

The deviation $g_{\mathbf{k}}^{\chi}$ is assumed to be linearly proportional to the applied electric field

$$g_{\mathbf{k}}^{\chi} = e\left(-\frac{\partial f_0^{\chi}}{\partial\epsilon_{\mathbf{k}}^{\chi}}\right)\mathbf{E}\cdot\mathbf{\Lambda}_{\mathbf{k}}^{\chi}. \tag{A6}$$

We fix the direction of the applied external electric field to be along $+\hat{z}$, i.e., $\mathbf{E} = E\hat{z}$. Therefore, only $\Lambda_{\mathbf{k}}^{\chi z} \equiv \Lambda_{\mathbf{k}}^{\chi}$ is relevant. Further, we rotate the magnetic field along the xz plane such that it makes an angle γ with respect to the $\hat{x}$ axis, i.e., $\mathbf{B} = B(\cos\gamma, 0, \sin\gamma)$. When $\gamma = \pi/2$, the electric and magnetic fields are parallel to each other. Similarly, the strain-induced chiral gauge field is rotated in the xz plane, i.e., $\mathbf{B_5}^{\chi} = \chi B_5(\cos\gamma_5, 0, \sin\gamma_5)$. When $\gamma_5 \neq \pi/2$, the electric and gauge field are noncollinear and this geometry will be useful in analyzing the strain-induced planar Hall effect. Thus, the net magnetic field at each valley becomes $\mathbf{B}^{\chi} \longrightarrow \mathbf{B} + \chi\mathbf{B_5}$.

Keeping terms only up to linear order in the electric field, Eq. (A5) takes the form

$$\mathcal{D}^{\chi}\left[v_{\mathbf{k}}^{\chi z} + \frac{eB}{\hbar}\sin\gamma\left(\mathbf{\Omega}^{\chi}\cdot\mathbf{v}_{\mathbf{k}}^{\chi}\right)\right] = \sum_{\eta}\sum_{\mathbf{k}'} W_{\mathbf{k}\mathbf{k}'}^{\eta\chi}\left(\Lambda_{\mathbf{k}'}^{\eta} - \Lambda_{\mathbf{k}}^{\chi}\right). \tag{A7}$$

In order to solve the above equation, we first define the valley scattering rate as

$$\frac{1}{\tau_{\mathbf{k}}^{\chi}} = \mathcal{V}\sum_{\eta}\int\frac{d^3\mathbf{k}'}{(2\pi)^3}\left(\mathcal{D}_{\mathbf{k}'}^{\eta}\right)^{-1} W_{\mathbf{k}\mathbf{k}'}^{\eta\chi}. \tag{A8}$$

Due to the tilting of the Weyl cones the azimuthal symmetry is destroyed even when the electric and magnetic fields are parallel to each other, and therefore all the integrations are performed over both θ and ϕ. The radial integration is simplified due to the delta function in Eq. (A4).

Substituting the scattering rate from Eq. (A4) in the above equation, we have

$$\frac{1}{\tau_{\mathbf{k}}^{\chi}} = \frac{\mathcal{V}N}{8\pi^2\hbar}\sum_{\eta}|U^{\chi\eta}|^2\iiint(k')^2\sin\theta'\mathcal{G}^{\chi\eta}(\theta,\phi,\theta',\phi')\delta \times\left(\epsilon_{\mathbf{k}'}^{\eta} - \epsilon_F\right)\left(\mathcal{D}_{\mathbf{k}'}^{\eta}\right)^{-1}dk'd\theta'd\phi', \tag{A9}$$

where N now indicates the total number of impurities, and $\mathcal{G}^{\chi\eta}(\theta,\phi,\theta',\phi') = \{1 + \chi\eta[\cos\theta\,\cos\theta' + \sin\theta\sin\theta'\cos(\phi - \phi')]\}$ is the Weyl chirality factor defined by the overlap of the wavefunctions. The Fermi wave-vector contour k^{χ} is evaluated by equating the energy expression with the Fermi energy. The three-dimensional integral in Eq. (A9) is reduced to just integration in ϕ' and θ'. The scattering time $\tau_{\mathbf{k}}^{\chi}$ depends on the chemical potential (μ), and is a function of the angular variables θ and ϕ:

$$\frac{1}{\tau_{\mu}^{\chi}(\theta,\phi)} = \mathcal{V}\sum_{\eta}\iint\frac{\beta^{\chi\eta}(k')^3}{\left|\mathbf{v}_{\mathbf{k}'}^{\eta}\cdot\mathbf{k}'^{\eta}\right|}\sin\theta'\mathcal{G}^{\chi\eta}\left(\mathcal{D}_{\mathbf{k}'}^{\eta}\right)^{-1}d\theta'd\phi', \tag{A10}$$

where $\beta^{\chi\eta} = N|U^{\chi\eta}|^2/4\pi^2\hbar^2$. The Boltzmann equation [Eq. (A7)] assumes the form

$$h_{\mu}^{\chi}(\theta,\phi) + \frac{\Lambda_{\mu}^{\chi}(\theta,\phi)}{\tau_{\mu}^{\chi}(\theta,\phi)} = \mathcal{V}\sum_{\eta}\iint\frac{\beta^{\chi\eta}(k')^3}{\left|\mathbf{v}_{\mathbf{k}'}^{\eta}\cdot\mathbf{k}'^{\eta}\right|}\sin\theta'\mathcal{G}^{\chi\eta}\left(\mathcal{D}_{\mathbf{k}'}^{\eta}\right)^{-1}\Lambda_{\mu}^{\eta}(\theta',\phi')d\theta'd\phi'. \tag{A11}$$

We make the following ansatz for $\Lambda_{\mu}^{\chi}(\theta,\phi)$:

$$\Lambda_{\mu}^{\chi}(\theta,\phi) = \left(\lambda^{\chi} - h_{\mu}^{\chi}(\theta,\phi) + a^{\chi}\cos\theta + b^{\chi}\sin\theta\,\cos\phi + c^{\chi}\sin\theta\,\sin\phi\right)\tau_{\mu}^{\chi}(\theta,\phi), \tag{A12}$$

where we solve for the eight unknowns $(\lambda^{\pm 1}, a^{\pm 1}, b^{\pm 1}, c^{\pm 1})$. The left-hand side in Eq. (A11) simplifies to $\lambda^{\chi} + a^{\chi}\cos\theta + b^{\chi}\sin\theta\,\cos\phi + c^{\chi}\sin\theta\,\sin\phi$. The right-hand side of Eq. (A11) simplifies to

$$\mathcal{V}\sum_{\eta}\beta^{\chi\eta}\iint f^{\eta}(\theta',\phi')\mathcal{G}^{\chi\eta}\big[\lambda^{\eta} - h^{\eta}_{\mu}(\theta',\phi') + a^{\eta}\cos\theta' + b^{\eta}\sin\theta'\cos\phi' + c^{\eta}\sin\theta'\sin\phi'\big]d\theta' d\phi', \tag{A13}$$

where the function

$$f^{\eta}(\theta',\phi') = \frac{(k')^3}{\left|\mathbf{v}^{\eta}_{\mathbf{k}'}\cdot\mathbf{k}'^{\eta}\right|}\sin\theta'\big(\mathcal{D}^{\eta}_{\mathbf{k}'}\big)^{-1}\tau^{\chi}_{\mu}(\theta',\phi'). \tag{A14}$$

The above equations, when written explicitly, take the form of seven simultaneous equations to be solved for eight variables. The final constraint comes from the particle-number conservation

$$\sum_{\chi}\sum_{\mathbf{k}} g^{\chi}_{\mathbf{k}} = 0. \tag{A15}$$

Equations (A12)–(A15) are solved together with Eq. (A10), simultaneously for the eight unknowns $(\lambda^{\pm 1}, a^{\pm 1}, b^{\pm 1}, c^{\pm 1})$. Due to the complicated nature of the equations, all the two-dimensional integrals with trespect to $\{\theta', \phi'\}$ and the solution of the simultaneous equations are performed numerically.

For the inversion asymmetric WSM with four Weyl nodes, the distribution function at each node can be represented by $f^{m}_{\mathbf{k}}$. Generalizing the formalism presented above, the collision integral must take into account scattering between multiple Weyl cones. Thus, $\mathcal{I}_{\rm coll}[f^{m}_{\mathbf{k}}]$ can be expressed as

$$\mathcal{I}_{\rm coll}\big[f^{m}_{\mathbf{k}}\big] = \sum_{p}\sum_{\mathbf{k}'} W^{mp}_{\mathbf{k},\mathbf{k}'}\big(f^{p}_{\mathbf{k}'} - f^{m}_{\mathbf{k}}\big), \tag{A16}$$

where p runs over all the nodes, and scattering rate $W^{mp}_{\mathbf{k},\mathbf{k}'}$ is given by

$$W^{mp}_{\mathbf{k},\mathbf{k}'} = \frac{2\pi}{\hbar}\frac{n}{\mathcal{V}}\left|\langle\psi^{p}_{\mathbf{k}'}|U^{mp}_{\mathbf{k}\mathbf{k}'}|\psi^{m}_{\mathbf{k}}\rangle\right|^2\delta\big(\epsilon^{p}_{\mathbf{k}'} - \epsilon_F\big). \tag{A17}$$

The scattering potential profile $U^{mp}_{\mathbf{k}\mathbf{k}'}$ can be chosen such that scattering between the nodes (internode) as well as within each node (intranode) is considered. Proceeding as before, we define $\tau^{m}_{\mathbf{k}}$ as

$$\frac{1}{\tau^{m}_{\mu}(\theta,\phi)} = \mathcal{V}\sum_{p}\iint\frac{\beta^{mp}(k')^3}{\left|\mathbf{v}^{p}_{\mathbf{k}'}\cdot\mathbf{k}'^{p}\right|}\sin\theta'\mathcal{G}^{mp}\big(\mathcal{D}^{p}_{\mathbf{k}'}\big)^{-1}d\theta' d\phi', \tag{A18}$$

and the Boltzmann equation becomes

$$h^{m}_{\mu}(\theta,\phi) + \frac{\Lambda^{m}_{\mu}(\theta,\phi)}{\tau^{m}_{\mu}(\theta,\phi)} = \mathcal{V}\sum_{p}\iint\frac{\beta^{mp}(k')^3}{\left|\mathbf{v}^{p}_{\mathbf{k}'}\cdot\mathbf{k}'^{p}\right|}\sin\theta'\mathcal{G}^{mp}\big(\mathcal{D}^{p}_{\mathbf{k}'}\big)^{-1}\Lambda^{p}_{\mu}(\theta',\phi')d\theta' d\phi'. \tag{A19}$$

Making the ansatz $\Lambda^{m}_{\mu}(\theta,\phi) = [\lambda^{m} - h^{m}_{\mu}(\theta,\phi) + a^{m}\cos\theta + b^{m}\sin\theta\,\cos\phi + c^{m}\sin\theta\,\sin\phi]\tau^{m}_{\mu}(\theta,\phi)$, and using the constraint for particle-number conservation, the Boltzmann equation is reduced to a system of 16 equations to be solved for 16 unknowns.

[1] R. Jackiw and S.-Y. Pi, Chiral Gauge Theory for Graphene, Phys. Rev. Lett. **98**, 266402 (2007).

[2] M. A. Vozmediano, M. Katsnelson, and F. Guinea, Gauge fields in graphene, Phys. Rep. **496**, 109 (2010).

[3] F. Guinea, M. Katsnelson, and A. Geim, Energy gaps and a zero-field quantum hall effect in graphene by strain engineering, Nat. Phys. **6**, 30 (2010).

[4] A. Cortijo, Y. Ferreirós, K. Landsteiner, and M. A. H. Vozmediano, Elastic Gauge Fields in Weyl Semimetals, Phys. Rev. Lett. **115**, 177202 (2015).

[5] D. I. Pikulin, A. Chen, and M. Franz, Chiral Anomaly from Strain-Induced Gauge Fields in Dirac and Weyl Semimetals, Phys. Rev. X **6**, 041021 (2016).

[6] A. G. Grushin, J. W. F. Venderbos, A. Vishwanath, and R. Ilan, Inhomogeneous Weyl and Dirac Semimetals: Transport in Axial Magnetic Fields and Fermi Arc Surface States from Pseudo-Landau Levels, Phys. Rev. X **6**, 041046 (2016).

[7] N. Levy, S. Burke, K. Meaker, M. Panlasigui, A. Zettl, F. Guinea, A. C. Neto, and M. F. Crommie, Strain-induced pseudo–magnetic fields greater than 300 tesla in graphene nanobubbles, Science **329**, 544 (2010).

[8] K.-Y. Yang, Y.-M. Lu, and Y. Ran, Quantum hall effects in a Weyl semimetal: Possible application in pyrochlore iridates, Phys. Rev. B **84**, 075129 (2011).

[9] A. A. Burkov, Anomalous Hall Effect in Weyl Metals, Phys. Rev. Lett. **113**, 187202 (2014).

[10] G. Sharma, P. Goswami, and S. Tewari, Nernst and magnetothermal conductivity in a lattice model of weyl fermions, Phys. Rev. B **93**, 035116 (2016).

[11] G. Sharma, C. Moore, S. Saha, and S. Tewari, Nernst effect in dirac and inversion-asymmetric weyl semimetals, Phys. Rev. B **96**, 195119 (2017).

[12] T. Liang, J. Lin, Q. Gibson, T. Gao, M. Hirschberger, M. Liu, R. J. Cava, and N. P. Ong, Anomalous Nernst Effect in the Dirac Semimetal Cd_3As_2, Phys. Rev. Lett. **118**, 136601 (2017).

[13] X. Wan, A. M. Turner, A. Vishwanath, and S. Y. Savrasov, Topological semimetal and fermi-arc surface states in the electronic structure of pyrochlore iridates, Phys. Rev. B **83**, 205101 (2011).

[14] S. Nandy, G. Sharma, A. Taraphder, and S. Tewari, Chiral Anomaly as the Origin of the Planar Hall Effect in Weyl Semimetals, Phys. Rev. Lett. **119**, 176804 (2017).

[15] G. Sharma and S. Tewari, Transverse thermopower in dirac and weyl semimetals, Phys. Rev. B **100**, 195113 (2019).

[16] S. L. Adler, Axial-vector vertex in spinor electrodynamics, Phys. Rev. **177**, 2426 (1969).

[17] H. B. Nielsen and M. Ninomiya, A no-go theorem for regularizing chiral fermions, Phys. Lett. B **105**, 219 (1981).

[18] H. B. Nielsen and M. Ninomiya, The Adler-Bell-Jackiw anomaly and Weyl fermions in a crystal, Phys. Lett. B **130**, 389 (1983).

[19] J. S. Bell and R. Jackiw, A PCAC puzzle: $\pi^0 \to \gamma\gamma$ in the σ-model, Nuovo Cimento A **60**, 47 (1969).

[20] V. Aji, Adler-Bell-Jackiw anomaly in Weyl semimetals: Application to pyrochlore iridates, Phys. Rev. B **85**, 241101(R) (2012).

[21] A. A. Zyuzin, S. Wu, and A. A. Burkov, Weyl semimetal with broken time reversal and inversion symmetries, Phys. Rev. B **85**, 165110 (2012).

[22] D. T. Son and N. Yamamoto, Berry Curvature, Triangle Anomalies, and the Chiral Magnetic Effect in Fermi Liquids, Phys. Rev. Lett. **109**, 181602 (2012).

[23] P. Goswami, G. Sharma, and S. Tewari, Optical activity as a test for dynamic chiral magnetic effect of Weyl semimetals, Phys. Rev. B **92**, 161110(R) (2015).

[24] K. Fukushima, D. E. Kharzeev, and H. J. Warringa, Chiral magnetic effect, Phys. Rev. D **78**, 074033 (2008).

[25] P. Goswami and S. Tewari, Axionic field theory of $(3+1)$-dimensional Weyl semimetals, Phys. Rev. B **88**, 245107 (2013).

[26] G. Volovik, On induced *CPT*-odd Chern-Simons terms in the $3+1$ effective action, J. Exp. Theor. Phys. Lett. **70**, 1 (1999).

[27] C.-X. Liu, P. Ye, and X.-L. Qi, Chiral gauge field and axial anomaly in a Weyl semimetal, Phys. Rev. B **87**, 235306 (2013).

[28] A. G. Grushin, Consequences of a condensed matter realization of lorentz-violating QED in Weyl semi-metals, Phys. Rev. D **86**, 045001 (2012).

[29] A. A. Zyuzin and A. A. Burkov, Topological response in Weyl semimetals and the chiral anomaly, Phys. Rev. B **86**, 115133(R) (2012).

[30] S. Ghosh, D. Sinha, S. Nandy, and A. Taraphder, Chirality-dependent planar hall effect in inhomogeneous Weyl semimetals, Phys. Rev. B **102**, 121105(R) (2020).

[31] G. Sharma, S. Nandy, K. V. Raman, and S. Tewari, Decoupling intranode and internode scattering in Weyl fermions, Phys. Rev. B **107**, 115161 (2023).

[32] A. Knoll, C. Timm, and T. Meng, Negative longitudinal magnetoconductance at weak fields in Weyl semimetals, Phys. Rev. B **101**, 201402(R) (2020).

[33] G. Sharma, S. Nandy, and S. Tewari, Sign of longitudinal magnetoconductivity and the planar hall effect in Weyl semimetals, Phys. Rev. B **102**, 205107 (2020).

[34] A. Ahmad and G. Sharma, Longitudinal magnetoconductance and the planar hall effect in a lattice model of tilted Weyl fermions, Phys. Rev. B **103**, 115146 (2021).

[35] D. Xiao, M.-C. Chang, and Q. Niu, Berry phase effects on electronic properties, Rev. Mod. Phys. **82**, 1959 (2010).

[36] B.-J. Yang and N. Nagaosa, Classification of stable three-dimensional dirac semimetals with nontrivial topology, Nat. Commun. **5**, 4898 (2014).

[37] T. Hashimoto, S. Kobayashi, Y. Tanaka, and M. Sato, Superconductivity in doped dirac semimetals, Phys. Rev. B **94**, 014510 (2016).

[38] G. Sharma, P. Goswami, and S. Tewari, Chiral anomaly and longitudinal magnetotransport in type-II Weyl semimetals, Phys. Rev. B **96**, 045112 (2017).

[39] K. Das and A. Agarwal, Linear magnetochiral transport in tilted type-I and type-II Weyl semimetals, Phys. Rev. B **99**, 085405 (2019).

[40] F. de Juan, M. Sturla, and M. A. H. Vozmediano, Space Dependent Fermi Velocity in Strained Graphene, Phys. Rev. Lett. **108**, 227205 (2012).

[41] Q.-D. Jiang, H. Jiang, H. Liu, Q.-F. Sun, and X.-C. Xie, Topological Imbert-Fedorov Shift in Weyl Semimetals, Phys. Rev. Lett. **115**, 156602 (2015).

[42] S. A. Yang, H. Pan, and F. Zhang, Chirality-Dependent Hall Effect in Weyl Semimetals, Phys. Rev. Lett. **115**, 156603 (2015).

[43] B. Z. Spivak and A. V. Andreev, Magnetotransport phenomena related to the chiral anomaly in Weyl semimetals, Phys. Rev. B **93**, 085107 (2016).

[44] M. Imran and S. Hershfield, Berry curvature force and lorentz force comparison in the magnetotransport of Weyl semimetals, Phys. Rev. B **98**, 205139 (2018).

[45] K.-S. Kim, H.-J. Kim, and M. Sasaki, Boltzmann equation approach to anomalous transport in a Weyl metal, Phys. Rev. B **89**, 195137 (2014).

[46] R. M. Dantas, F. Peña-Benitez, B. Roy, and P. Surówka, Magnetotransport in multi-weyl semimetals: A kinetic theory approach, J. High Energy Phys. 12 (2018) 69.

[47] A. Johansson, J. Henk, and I. Mertig, Chiral anomaly in type-I Weyl semimetals: Comprehensive analysis within a semiclassical fermi surface harmonics approach, Phys. Rev. B **99**, 075114 (2019).

[48] K. Das and A. Agarwal, Berry curvature induced thermopower in type-I and type-II Weyl semimetals, Phys. Rev. B **100**, 085406 (2019).

[49] A. Cortijo, Linear magnetochiral effect in Weyl semimetals, Phys. Rev. B **94**, 241105(R) (2016).

[50] V. A. Zyuzin, Magnetotransport of Weyl semimetals due to the chiral anomaly, Phys. Rev. B **95**, 245128 (2017).

[51] H. Bruus and K. Flensberg, *Many-body Quantum Theory in Condensed Matter Physics: An Introduction* (Oxford University Press, Oxford, 2004).